UNIVERSITY OF CALIFORNIA SAN DIEGO

Fully-automated, Fast Evaluation of CineCT for Detection of Wall Motion Abnormality using both Global and Regional Metrics of Function

A Thesis submitted in partial satisfaction of the requirements
for the degree Master of Science

in

Bioengineering

by

Hui Li

Committee in charge:

Professor Francisco Contijoch, Chair
Professor Seth Kligerman
Professor Elliot McVeigh

2022

The Thesis of Hui Li is approved, and it is acceptable in quality and form for publication on microfilm and electronically.

University of California San Diego

2022

TABLE OF CONTENTS

THESIS APPROVAL PAGE iii

TABLE OF CONTENTS iv

LIST OF FIGURES vi

LIST OF TABLES vii

LIST OF ABBREVIATIONS viii

ACKNOWLEDGEMENTS ix

ABSTRACT OF THE THESIS xi

CHAPTER 1 BACKGROUND 1

1.1 CARDIAC CT 1
1.2 DEEP LEARNING ANALYSIS OF CARDIAC IMAGES 3
1.3 LONGITUDINAL SHORTENING 5
1.4 MITRAL ANNULAR PLANE SYSTOLIC EXCURSION (MAPSE) 7

CHAPTER 2 METHODS 9

2.1 STUDY POPULATION 9
2.2 AUTOMATED ESTIMATION OF LONGITUDINAL SHORTENING ALONG EACH LONG-AXIS PLANE 10
2.3 EXPERT IDENTIFICATION OF WALL MOTION ABNORMALITIES 11
2.4 PAPILLARY MUSCLE ARTIFACTS AND CORRECTION APPROACHES 13
2.5 DETERMINATION OF LS CUTOFFS IN TRAINING COHORT AND EVALUATION IN TESTING COHORT 15
2.6 AUTOMATED ESTIMATION OF MAPSE AND ALTERNATIVES 16
2.7 STATISTICAL EVALUATION 17

CHAPTER 3 RESULTS 18

3.1 PATIENT COHORT 18
3.2 CORRECTION FOR PAPILLARY MUSCLE ARTIFACTS 19
3.3 DETERMINATION OF LS CUTOFFS AND CLASSIFICATION PERFORMANCE IN TRAINING COHORT 20
3.4 PER-STUDY AND PER-VIDEO CLASSIFICATION PERFORMANCE IN TESTING COHORT 22
3.5 MAPSE 24

CHAPTER 4 DISCUSSION 27

4.1 CONCLUSIONS 27

4.2 MAPSE 28
4.3 LIMITATIONS 28
4.4 PERFORMANCE OF LS CLASSIFICATION WITH EXPERT CONCORDANCE/DISCORDANCE ... 29
4.5 LS ESTIMATION MAY BE LIMITED DUE TO FORESHORTENING 29

REFERENCES 31

LIST OF FIGURES

Figure 1.1: Coronary CT angiogram is used for diagnosing coronary artery disease 1

Figure 1.2: ECG-gated cardiac CT, showing heart motion at end-diastole and end-systole frames. 2

Figure 1.3: Correlation plot and Bland-Altman plot showing agreement between LS measured using cardiac CT and echocardiography. 2

Figure 1.4: SQUEEZE analysis estimates regional shortening. 3

Figure 1.5: Deep learning framework is used to obtain LV and LA segmentation on long axis views. 4

Figure 1.6: Performance of DL framework in finding the imaging planes as compared with manual planning. 5

Figure 1.7: Longitudinal shortening is measured as the percent change in LV endocardium length between end-diastole and end-systole. 6

Figure 1.8: MAPSE is measured as the mean displacement of the left and right mitral valve points between end-diastole and end-systole, averaged between three LAX views. 7

Figure 2.1: Endocardium is measured by subtracting LV/LA boundary from LV perimeter. 11

Figure 2.2: Instruction for expert readers on WMA labeling. 12

Figure 2.3: Measurement of endocardial perimeter based on the blood pool segmentation is susceptible to artifacts created by the papillary muscles. Smoothing with convex hull and convex hull + curve fitting was applied. 15

Figure 2.4: MAPSE and alternative MAPSE measurements. 16

Figure 3.1: Agreement between LS and FAC increases with use of the convex hull and perimeter curve fitting. 20

Figure 3.2: ROC curves for WMA classification using LS in the training cohort. 21

Figure 3.3: MAPSE correlation plot with EF. 25

Figure 3.4: ROC plot for WMA classification using MAPSE in the training cohort. 25

LIST OF TABLES

Table 2.1: AHA segments corresponding to each LAX view. 13

Table 3.1: Patient Cohort Information..... 18

Table 3.2: Use of training cohort for identification of LS cutoffs for WMA detection using the curve fitting approach..... 22

Table 3.3: Performance of LS in the testing cohort using the curve-fitting approach. 23

Table 3.4: Confusion matrix for 2-Chamber, 3-Chamber, 4-Chamber views, all views and per-study identification of WMA, using individual threshold..... 24

Table 3.5: Confusion matrix for 2-Chamber, 3-Chamber, 4-Chamber views, all views and per-study identification of WMA, using single threshold. 24

Table 3.6: Use of training cohort for identification of MAPSE cutoffs for WMA detection and performance of MAPSE in the testing cohort using the conventional approach. 26

LIST OF ABBREVIATIONS

LS	Longitudinal Shortening
MAPSE	Mitral Annular Plane Systolic Excursion
LAX	Long Axis
DL	Deep Learning
EF	Ejection Fraction
LVEF	Left Ventricular Ejection Fraction.
FAC	Fractional Area Change
WMA	Wall Motion Abnormality
2-CH	2-Chamber
3-CH	3-Chamber
4-CH	4-Chamber
ROC	Receiver Operating Characteristic
AUC	Area Under the Receiver Operating Characteristic Curve
IQR	Interquartile Range
Conv hull	Convex hull
Accu	Accuracy
Sens	Sensitivity
Spec	Specificity
PPV	Positive Predictive Value

ACKNOWLEDGEMENTS

Thanks to Dr. Francisco Contijoch for all the guidance and support through the course of this research.

Thanks to my thesis committee members Dr Contijoch, Dr Kligerman and Dr McVeigh.

Thanks to Zhennong Chen for his prior work on the deep learning framework.

Thanks to Andrew Kahn, Seth Kligerman and Hari Narayan for providing expert WMA classification for the research data.

Thanks to my labmates and friends from the Contijoch Research Lab.

Thanks to my family and friends for their love and support.

Chapter 1, in part, has been submitted for publication of the material as it may appear in Frontiers, 2022, Hui Li; Zhennong Chen; Andrew M Kahn; Seth Kligerman; Hari K Narayan; Francisco J Contijoch. The thesis author was the primary researcher and author of this paper. Content of this chapter has, in part, been presented at SCCT.

Chapter 2, in part, has been submitted for publication of the material as it may appear in Frontiers, 2022, Hui Li; Zhennong Chen; Andrew M Kahn; Seth Kligerman; Hari K Narayan; Francisco J Contijoch. The thesis author was the primary researcher and author of this paper. Content of this chapter has, in part, been presented at SCCT.

Chapter 3, in part, has been submitted for publication of the material as it may appear in Frontiers, 2022, Hui Li; Zhennong Chen; Andrew M Kahn; Seth Kligerman; Hari K Narayan; Francisco J Contijoch. The thesis author was the primary researcher and author of this paper. Content of this chapter has, in part, been presented at SCCT.

Chapter 4, in part, has been submitted for publication of the material as it may appear in Frontiers, 2022, Hui Li; Zhennong Chen; Andrew M Kahn; Seth Kligerman; Hari K Narayan; Francisco J Contijoch. The thesis author was the primary researcher and author of this paper.

ABSTRACT OF THE THESIS

Fully-automated, Fast Evaluation of CineCT for Detection of Wall Motion Abnormality using both Global and Regional Metrics of Function

by

Hui Li

Master of Science in Bioengineering

University of California San Diego, 2022

Professor Francisco Contijoch, Chair

4D cardiac CT is increasingly used to evaluate cardiac dynamics. Echocardiography and CMR have demonstrated the utility of longitudinal shortening (LS) measures. We demonstrate the ability of a recently published deep learning framework to automatically and accurately measure LS from CT for detection of wall motion abnormalities (WMA) and Mitral Annular Plane Systolic Excursion (MAPSE).

100 clinical cineCT studies were evaluated by three experienced cardiac CT readers for presence of WMA: 50 for method development and 50 for testing. Previously developed convolutional neural network was used to automatically segment the LV bloodpool and to define the 2CH, 3CH, and 4CH long-axis imaging planes. LS was measured as the perimeter of the bloodpool for each long-axis plane. Two smoothing approaches were developed to avoid artifacts. The impact of the smoothing was evaluated by comparing LS estimates to LV ejection fraction and the fractional area change of the corresponding view.

Our approach successfully analyzed 48/50 patients in the training cohort and 47/50 in the testing cohort. Smoothing significantly improved agreement between LS and fractional area change (R^2: 2CH=0.38 vs 0.88 vs 0.92). The optimal single LS cutoff for identification of WMA in all LAX views was -17.0% in the training cohort. This led to correct labeling of 85% of the views in the testing cohort. Per-study accuracy was 83% (79% sensitivity and 86% specificity). LS values accurately identify regional wall motion abnormalities and may be used to complement standard visual assessments. MAPSE showed less utility in classification of WMA compared with LS.

CHAPTER 1 BACKGROUND

1.1 Cardiac CT

Cardiac computed tomography (CT) is increasingly used to evaluate both coronary artery anatomy [1],[2] and cardiac function [3]. For example, **Figure 1.1** shows how coronary arteries can be visualized by reformatting a CT angiogram while **Figure 1.2** shows two timeframes from an ECG-gated acquisition which shows cardiac motion.

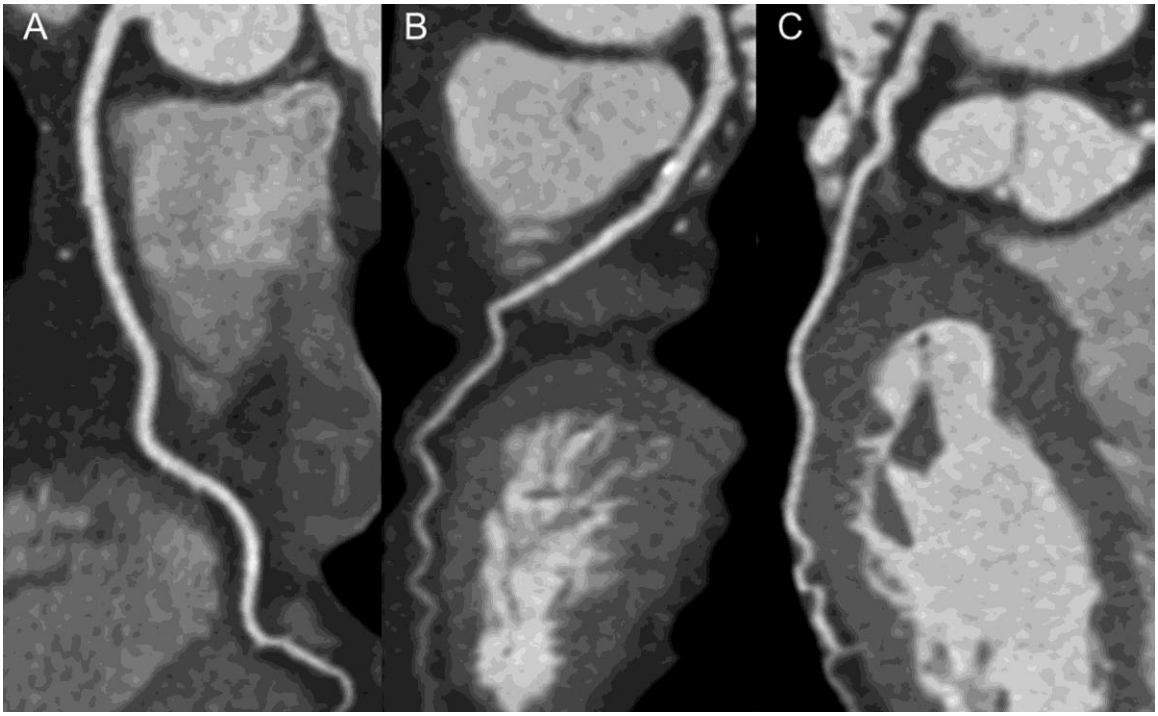

Figure 1.1: Coronary CT angiogram is used for diagnosing coronary artery disease. [4]

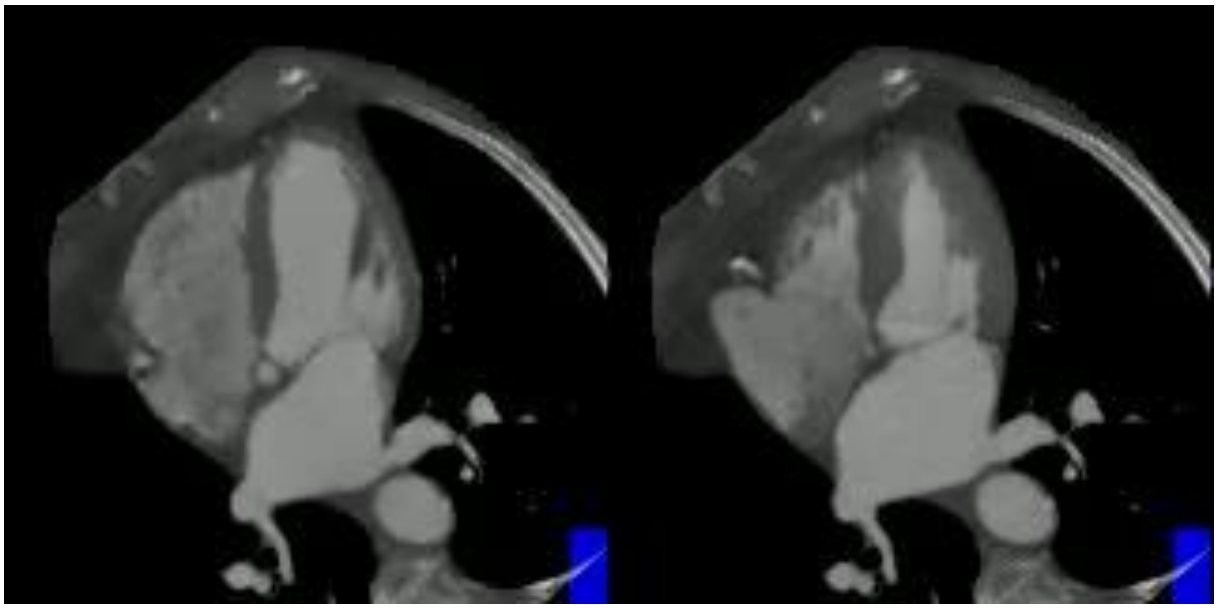

Figure 1.2: ECG-gated cardiac CT, showing heart motion at end-diastole and end-systole frames.

Recent work has shown that ECG-gated CT can detect regional wall motion abnormalities and that findings agree with echocardiography [5, 6] and CMR [7, 8]. **Figure 1.3** shows the agreement between CT and echo-derived longitudinal shortening as reported by Buss et al [6].

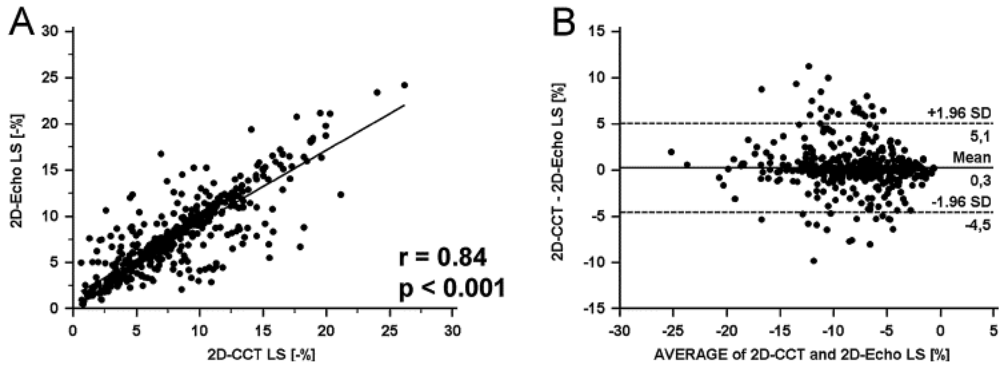

Figure 1.3: (A) Correlation plot and (B) Bland-Altman plot showing agreement between LS measured using cardiac CT and echocardiography.

While our group and others have developed quantitative methods to evaluate of cardiac function on 4D CT data, they can often require significant computational processing such as 3D

segmentation or measurement of wall thickening. **Figure 1.4** shows how the regional shortening of the endocardium can be measured to identify areas of impairment.

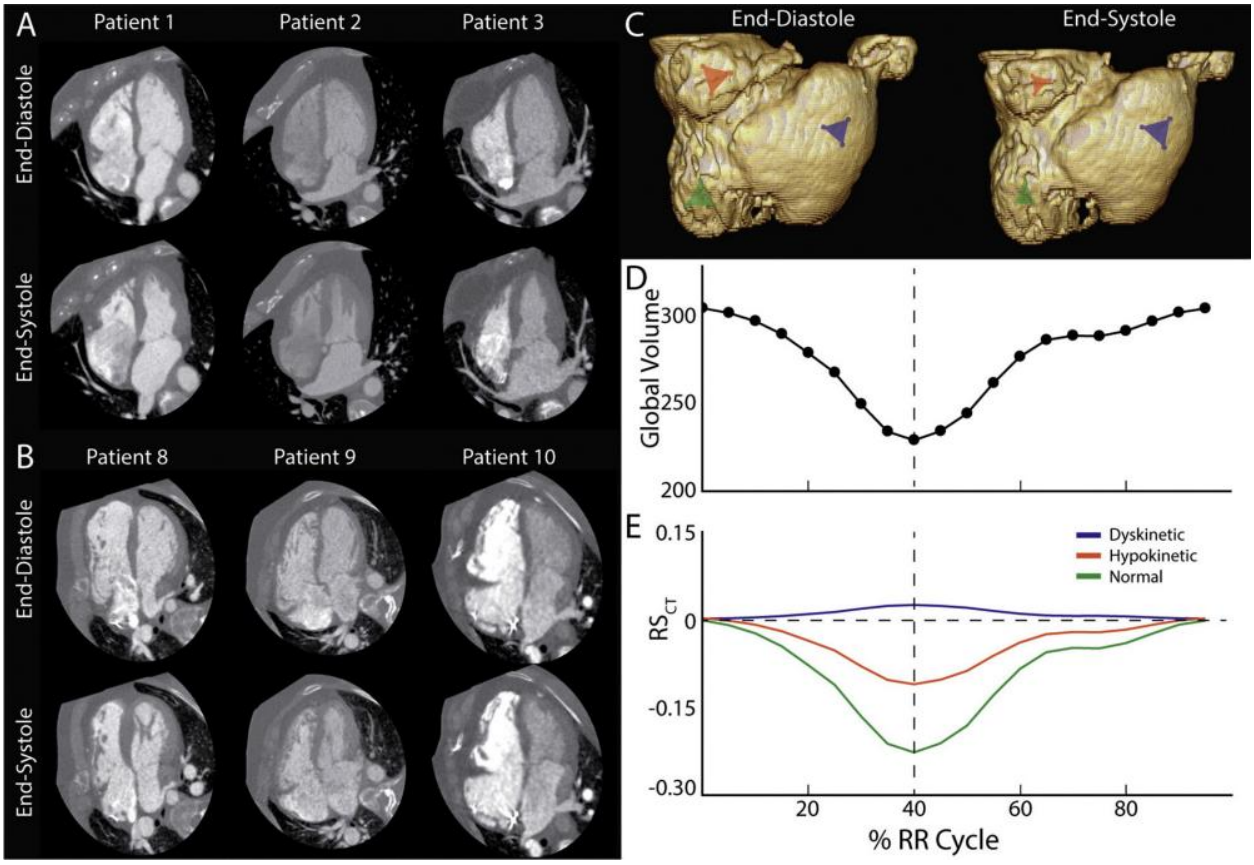

Figure 1.4: SQUEEZE analysis estimates regional shortening [9]. (C) shows three areas being measured, and (E) shows regional shortening of these areas.

1.2 Deep Learning Analysis of Cardiac Images

Recently, a deep learning framework has been shown to automatically and accurately identify the long-axis planes within a 4D CT dataset and, using the same architecture, segment the LA and LV blood pools [10]. **Figure 1.5** shows the structure of the DL framework. Using a modified U-net architecture, the algorithm was first trained to perform blood pool segmentation of the left atrium and ventricle. Then, an output was added after the last max-pooling layer in the downsampling path. This was used to regress the translation vector (define the spatial position of

the long-axis view) and direction vectors (define the orientation of the view) for each of the long-axis views.

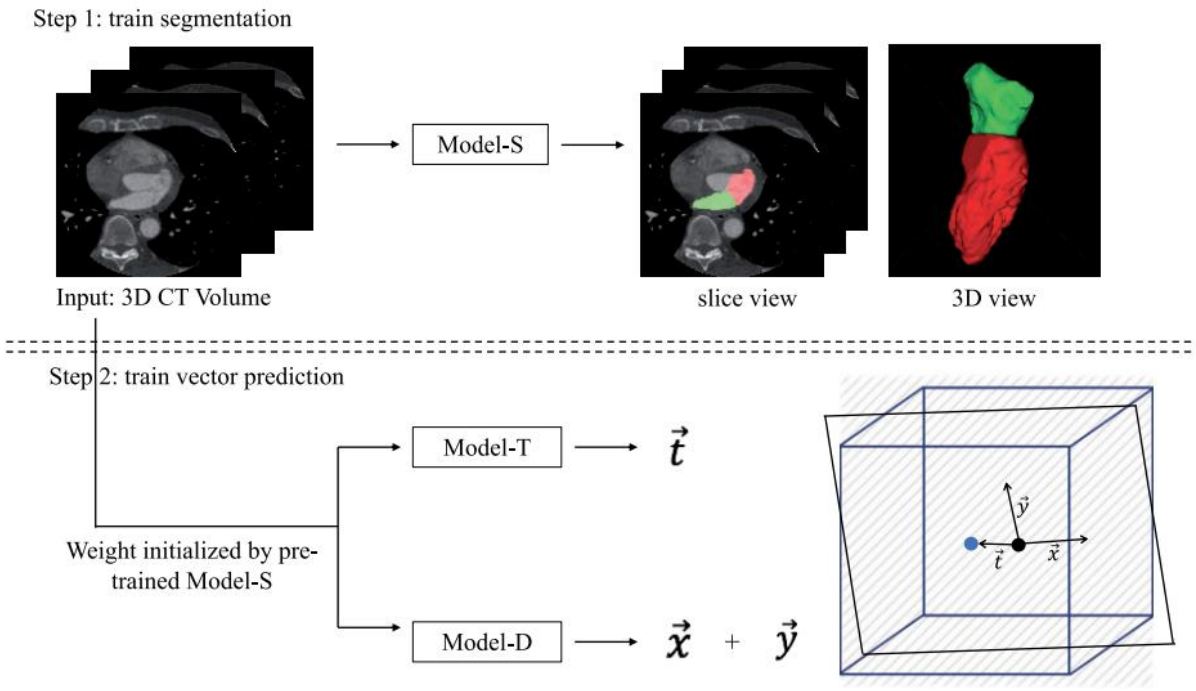

Figure 1.5: Deep learning framework is used to obtain LV and LA segmentation on long axis views. Model-S segments LV and LA bloodpool from 3D CT data, and Model-T and Model-D determine the position and orientation of long axis planes. [10]

Specifically, long-axis views generated via the DL method were in close agreement with user-defined planes and >94% of views were diagnostically accurate. Performance of the DL-defined imaging planes is shown in **Figure 1.6**.

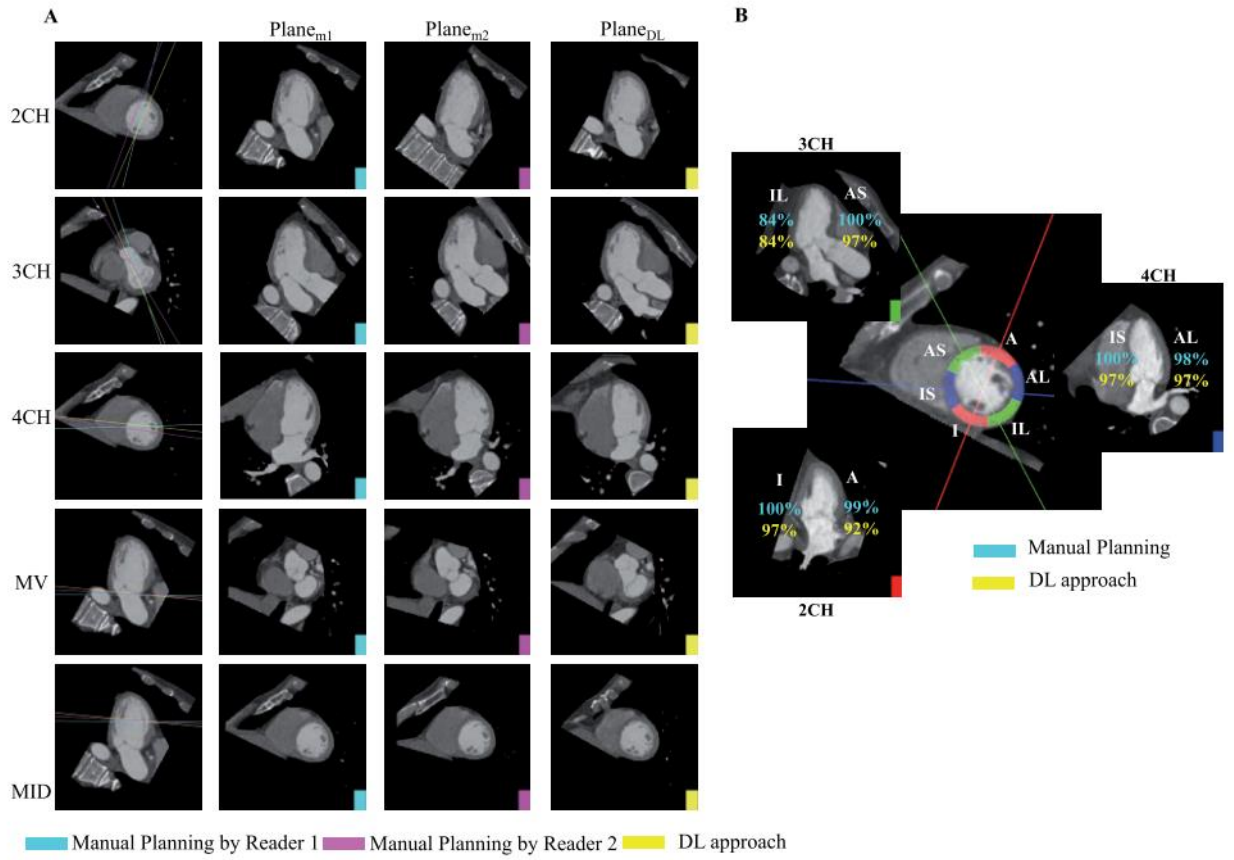

Figure 1.6: Performance of DL framework in finding the imaging planes as compared with manual planning. (A) Imaging planes as determined by 2 expert readers and the DL approach. (B) Percentage of cases where LAX views intersect correct walls. DL-derived planes agree closely to manual planes. [10]

By segmenting both the LV and LA blood pools, this creates the opportunity to evaluate LS by measuring the LV endocardial perimeter (after removal of the mitral valve plane). This also creates the opportunity to evaluate mitral annular plane systolic excursion by tracking movement of the mitral valve plane.

1.3 Longitudinal Shortening

Longitudinal shortening (LS) is defined as the change in LV endocardium length between end-diastole and end-systole. **Figure 1.7** shows how it can be derived from long-axis images.

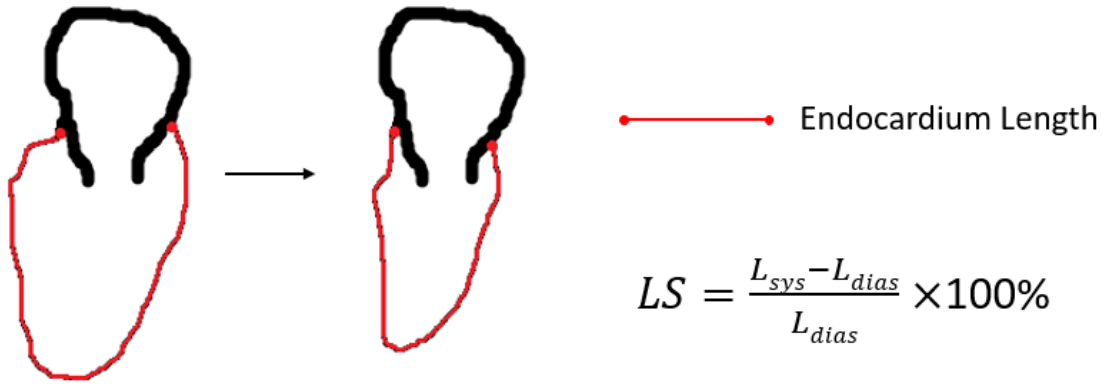

Figure 1.7: Longitudinal shortening is measured as the percent change in LV endocardium length between end-diastole and end-systole

It can be measured using echocardiography [11] or cardiac magnetic resonance [12], and has been proven useful in evaluating patients at risk of chemotherapy cardiotoxicity [13] and those with aortic stenosis [14, 15], cardiac amyloidosis [16] atrial fibrillation [17], and heart failure [18]. In revascularized STEMI patients, CMR-based LS was superior and incremental to LVEF and scar size in the prediction of MACE [19].

LS can also be used as a quantitative metric to improve detection of wall motion abnormalities (WMA) [20, 21] and in the setting of infarction WMA have been shown to be an independent predictor of adverse events [22, 23]. Further, in patients without overt cardiovascular disease, presence of a WMA leads to a 2.4-3.4 higher risk of cardiovascular morbidity and mortality, independent of established risk factors [24].

While several automated methods have been developed for the evaluation of cardiac chamber size and global function [25–28], automated estimation of LS from 4DCT is not currently available as it requires the combination of manual/semi-automated reformatting of the 4D dataset into long-axis imaging planes as well as delineation of the endocardial boundary across frames [29].

1.4 Mitral Annular Plane Systolic Excursion (MAPSE)

The displacement of the mitral annulus (MAPSE) has been correlated to LV function, which is important for early detection of heart dysfunction. **Figure 1.8** shows how it can be measured using long-axis images.

In patients with heart failure, MAPSE can be reduced despite preserved LVEF and therefore more sensitive in early detection of abnormal LV function [30]. It has been used as a complimentary measure to EF. MAPSE is also less dependent on image quality compared with EF or LS [31]. Currently MAPSE is measured using echocardiography and CMR, and while manual estimation is simple, automated measurement of MAPSE from cardiac CT has not been established.

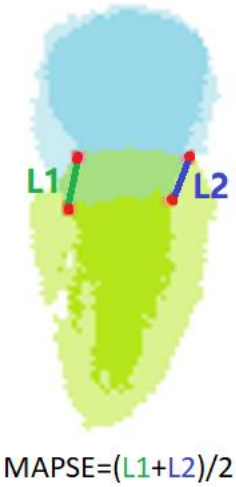

Figure 1.8: MAPSE is measured as the mean displacement of the left and right mitral valve points between end-diastole and end-systole, averaged between three LAX views.

In this thesis, we evaluate the ability of a recently developed deep learning algorithm to be adapted to obtain automated LS estimates from each long-axis view and MAPSE estimates

from three long axis views. To test the clinical utility of our approach, we evaluated whether automatic LS and MAPSE can be used to detect WMA in a set of 100 clinical cases which were visually analyzed by three trained experts for the presence of WMA. We created two cohorts (n=50 training and n=50 testing cases). We used the training cohort to determine the optimal LS and MAPSE threshold for detecting WMA and report accuracy in the independent testing cohort.

Acknowledgements

Chapter 1, in part, has been submitted for publication of the material as it may appear in Frontiers, 2022, Hui Li; Zhennong Chen; Andrew M Kahn; Seth Kligerman; Hari K Narayan; Francisco J Contijoch. The thesis author was the primary researcher and author of this paper. Content of this chapter has, in part, been presented at SCCT.

CHAPTER 2 METHODS

2.1 Study Population

Our goal was to create a dataset which had images with and without wall motion abnormalities. Having a near even distribution would allow for better evaluation of our methods. Therefore, we took several steps to build nearly balanced training and testing cohorts.

The initial dataset included 505 ECG-gated contrast enhanced cardiac CT studies acquired between April 2018 and December 2020 which had (1) full R-wave to R-wave (RR) coverage and (2) an imaging report including the explicit mention of cardiac function as normal or abnormal (either globally or regionally). All CT scans were performed on the same wide-detector CT scanner with 256 detector rows and 16cm z-axis coverage (Revolution scanner, GE Healthcare, Chicago IL). Visual inspection resulted in 97 studies being excluded due to poor image quality, lead artifacts which impacted the LV blood pool, or failure to visualize the entire LV.

Imaging reports were used as a first attempt to balance the study cohort. Two hundred and forty six studies were reported to have “normal” function in the report while 162 were classified as having “abnormal” function. To balance between patients with normal and abnormal function, the studies with normal function acquired at the end of the review period (acquired between August and December 2020, n=66 studies total) were excluded. From the remaining n=180 studies with normal function and n=162 studies with abnormal function, 100 studies were randomly selected: 50 are used for method development (training cohort) and 50 are for validation.

The final designation of a study as normal or abnormal was performed by three experts ss described below. Experts visually inspected the short and long-axis movies to identify whether

any area was considered abnormal. Therefore, this initial step was aimed at arriving at a relatively balanced distribution of normal and abnormal studies without introducing bias into the selection process.

All studies had functional phases reconstructed at 10% RR intervals using the vendor default cardiac function image reconstruction method. Images were reconstructed on a 512x512 pixel matrix in the axial plane over a field of view of 240 +- 20 mm with 0.625 mm slice thickness.

The causes for the CT scans in these 100 patients were: n=33 for pre-procedure assessment of pulmonary vein isolation, n=50 for suspected coronary artery disease, n=9 for preoperative assessment of left ventricular assist device placement, n=5 for preoperative assessment of transcatheter aortic valve replacement, and n=3 for preoperative assessment of cancer chemotherapy.

2.2 Automated Estimation of Longitudinal Shortening Along Each Long-Axis Plane

Using the deep learning network by Chen at al., automated blood pool and long-axis views were generated. LV and LA bloodpool segmentation at each of the LAX views were obtained for our patient cohort and input into a program in Matlab for automated estimation of LS. The program estimates LV endocardium by extracting the perimeter of the LV bloodpool and excluding the part adjacent to the LA bloodpool (which corresponds to the mitral valve). Endocardium length is recorded for each frame in a heart cycle, and a strain plot is generated. The program also determines end-systole by analyzing LV volume data and finding the frame

that corresponds to smallest LV volume. LS is then calculated automatically using endocardium length at end-diastole and end systole.

Figure 2.1: Endocardium is measured by subtracting LV/LA boundary from LV perimeter.

2.3 Expert Identification of Wall Motion Abnormalities

The CT studies were independently evaluated for WMA by three cardiovascular imagers with 15 years, 14 years and 5 years of experience interpreting cardiac studies. For each study, experts were provided movie reformats of the 4D CT dataset along both short- and long-axis views (an example is shown in **Figure 2.2A**), and they were asked to fill out wall motion in three long-axis pictures, at 16 AHA segment locations (not including the apical segment), in a blinded fashion, as either 1) normal, 2) hypokinetic, 3) akinetic or dyskinetic (**Figure 2.2B**). This aims to establish a "ground truth" reference for presence and location of WMA in all the studies.

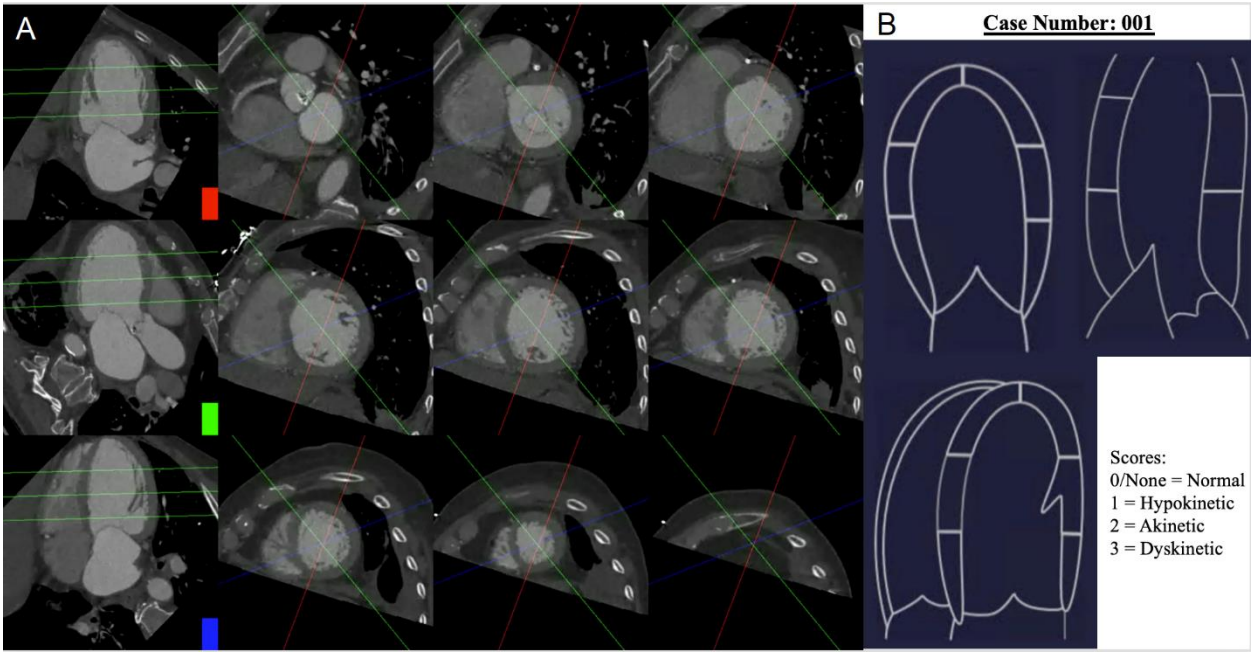

Figure 2.2: Instruction for expert readers on WMA labeling. (A) Plane movie in both long- and short-axis views were provided to experts for each study. (B) Long-axis tables with 16 AHA segments for experts to fill in wall motion score.

This led to 1600 segments being labeled. Given the limited number of hypo- and dyskinetic segments and the interobserver variability, we combined hypokinetic, akinetic and dyskinetic labels into a single “abnormal” class and only performed per-imaging plane and per-study comparison. A long-axis view was considered abnormal if it contained one or more AHA segments that were labeled abnormal.

Table 2.1: AHA segments corresponding to each LAX view.

Long Axis View	AHA Segments Involved
2-CH	Basal Inferior, Basal Anterior, Mid Anterior, Mid Inferior, Apical Anterior, Apical Inferior
3-CH	Basal Anteroseptal, Basal Inferolateral, Mid Anteroseptal, Mid Inferolateral, Apical Anterior, Apical Lateral
4-CH	Basal Inferoseptal, Basal Anterolateral, Mid Anterolateral, Mid Inferoseptal, Apical Septal, Apical Lateral

Given that 3 long axis videos were made per patient, this resulted in 300 long-axis videos (150 in the training and 150 in the testing cohort), each with a normal or abnormal designation. A CT study was classified as abnormal if it had one or more abnormal LAX video. For comparison to our DL-based approach, the three expert scores were combined such that a segment was labeled abnormal if there was agreement by 2 or more readers.

2.4 Papillary Muscle Artifacts and Correction Approaches

The LV bloodpool segmentations generated by the deep learning framework does not include volume of the papillary muscles. These papillary muscles appear on the long axis plane segmentations as concave areas in the LV, and measuring LS directly from the segmentation was susceptible to artifacts. An example is shown in **Figure 2.3**. To reduce the effect of artifacts, two smoothing approaches were implemented and evaluated. First, the concave areas created by the papillary muscles were “filled in” by using the binary “close” function with a disk of 10 pixels

and then fitting a convex hull to the perimeter of the endocardial bloodpool for each frame [32]. An example result of this approach is shown in **Figure 2.3**.

However, there are limitations with this approach. First, the perimeter measured depends on the "texture" of the surface. This may lead to overestimation of the perimeter. Second, use of the convex hull fills the area of the papillary muscle insertion with a straight line that may underestimate the perimeter. To address these limitations, we fit a "natural" spline curve [33] to the perimeter obtained after via closing and filling via the convex hull. Fitting was performed after downsampling the curve by a user-defined factor of 5. The result, in the same patient as above, is shown in **Figure 2.3**.

For the three methods, LS was calculated as the percent change in length between end-diastole and end-systole. To sanity check the quality of LS estimation and effect of smoothing, correlation between the LS estimate and the LV ejection fraction and the fractional area change (FAC) of the corresponding view were compared for the unsmooth LS result as well as LS after convex hull and convex hull + curve fitting refinement.

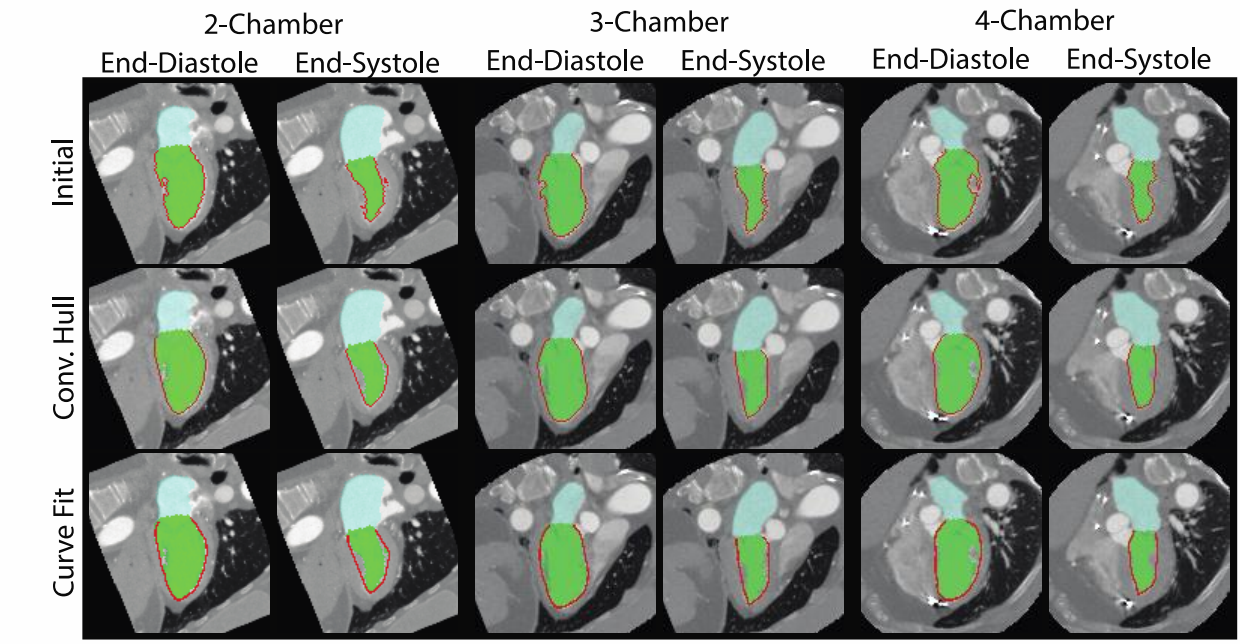

Figure 2.3: Measurement of endocardial perimeter based on the blood pool segmentation is susceptible to artifacts created by the papillary muscles (1st row). Smoothing with convex hull (2nd row) and convex hull + curve fitting (3rd row) was applied.

2.5 Determination of LS Cutoffs in Training Cohort and Evaluation in Testing Cohort

We varied the threshold used to determine whether a LS value (for a particular view) accurately detected the presence of a WMA, as determined by our three experts. Using the training cohort (n=50), we identified the thresholds which optimized performance for each LAX view and identified the single threshold that had peak performance when applied to all LAX views. Optimal performance was based on the threshold corresponding to the upper left most point on the receiver operating characteristic (ROC) curve.

The accuracy, sensitivity, and specificity of these thresholds were then evaluated in an independent cohort of n=50 patients.

2.6 Automated Estimation of MAPSE and Alternatives

Deep learning analysis of cardiac CT also enables automated estimation of MAPSE. The same Matlab program is used to automatically extract mitral valve endpoints from each long axis video in the training and testing cohort and estimate MAPSE. MAPSE is measured as the displacement of mitral valve endpoints between end-diastole and end-systole, averaged between left and right mitral valve point then averaged between three long axis views [34]. Alternatively, Midpoint-MAPSE is measured as the displacement of the mitral valve midpoint (between left and right mitral valve points) averaged between three long axis views. Longitudinal-MAPSE is measured similar to MAPSE, but displacement is measured only in longitudinal direction.

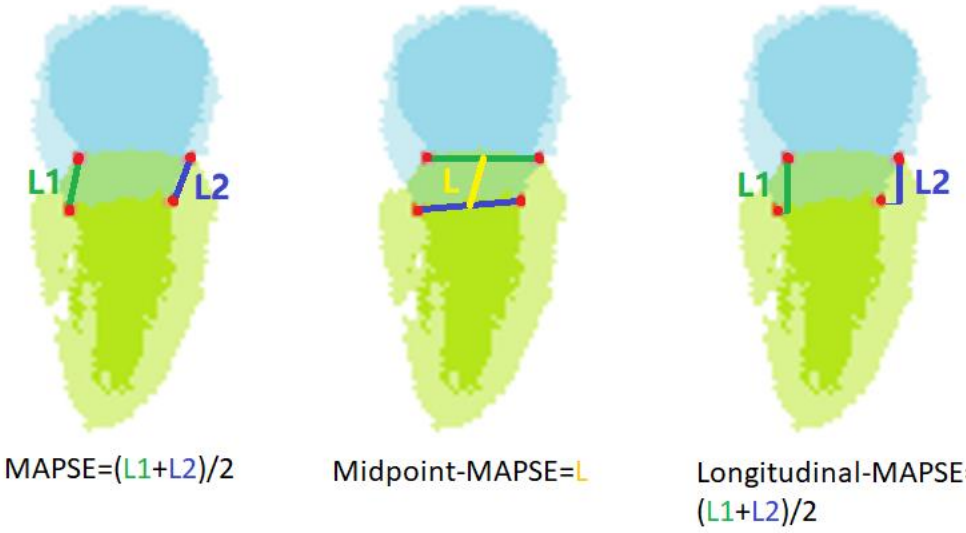

Figure 2.4: MAPSE and alternative MAPSE measurements.

MAPSE and alternative MAPSE measurements are evaluated by comparing with LV ejection fraction. Optimal MAPSE cutoff for detecting WMA is determined using the training cohort based on the threshold corresponding to the upper left most point on the receiver operating characteristic (ROC) curve. The accuracy, sensitivity, and specificity of these thresholds were then evaluated in the testing cohort.

2.7 Statistical Evaluation

Normally distributed values are expressed as mean ± standard deviation while non-normal values are reported using the median and interquartile range (IQR). Two-tailed categorical z-test was used to compare data proportions (e.g., proportions of abnormal videos) in the training and a testing cohort. To compare R^2 values between FAC and LS for different smoothing methods in dependent samples, the Fisher's r-to-z transformation was utilized to determine statistical significance. Statistical significance was set at $P \leq 0.05$.

The ability of LS to detect WMA was compared against the expert labeled ground truth label and was reported via confusion matrix and Cohen's kappa value. Both per-long axis video and per-study comparisons were performed. Readers reviewed long-axis and short-axis movies of the cardiac cycle and labeled each AHA segment. A video was labeled as abnormal if it had one or more abnormal AHA segments present. A study was defined as abnormal if it had one or more long-axis videos labeled as abnormal. Interobserver agreement in terms of labeling wall motion as normal or abnormal between three experts was measured using Fleiss's Kappa [35] since there were more than two observers.

Acknowledgements

Chapter 2, in part, has been submitted for publication of the material as it may appear in Frontiers, 2022, Hui Li; Zhennong Chen; Andrew M Kahn; Seth Kligerman; Hari K Narayan; Francisco J Contijoch. The thesis author was the primary researcher and author of this paper. Content of this chapter has, in part, been presented at SCCT.

CHAPTER 3 RESULTS

3.1 Patient Cohort

61 subjects were men and 49 were woman with a mean age of 59 ± 14. The LV blood pool had a median intensity of 530 HU (IQR: 435 to 663). Out of the 1600 segments evaluated, 27% (432/1600) were labeled abnormal by experts. This led to 41% (123/300) long-axis videos and 44 studies with at least one abnormal AHA segment. There were no significant differences (all P values > 0.05) between the training and testing cohorts in terms of the percentages of sex, abnormal videos, abnormal CT studies.

Table 3.1: Patient Cohort Information. LVEF: left ventricular ejection fraction.

	Entire Dataset	**Training Cohort**	**Validation Cohort**
Cohort Size, n	100	50	50
Age, years	59 ± 14	59 ± 15	59 ± 13
Male, %	61	58	64
Median LVEF, %	62.4 (IQR: 41.7 – 69.3)	62.1 (IQR: 38.9 – 69.6)	63.8 (IQR: 45.1 – 68.5)
Abnormal segments	27% (432/1600)	27% (219/800)	27% (213/800)
Abnormal LAX views	41% (123/300)	43% (64/150)	39% (59/150)
Normal studies, n	56	28	28

Automated, DL approach successfully analyzed 48/50 patients in the training cohort and 47/50 in the testing cohort. The 5 failures occurred due to incorrect prediction of long-axis planes. In 2 of these 5 cases, the patients had a metal prosthetic mitral valve.

84.6% (1,354/1,600) of segments were labeled identically by all three reviewers. The interobserver agreement amongst the three observers in terms of classifying a segmental wall motion into normal vs. abnormal, measured via Fleiss's Kappa, was 0.746, which indicates strong agreement. Fleiss's Kappa for agreement in classifying a LAX video was 0.800 (0.791, 0.811, and 0.797 for the 2, 3 and 4CH views, respectively) and the value for classifying a patient was 0.786.

3.2 Correction for Papillary Muscle Artifacts

The papillary muscle artifacts and the rough endocardial surface led to poor agreement between the fractional area change and LS when LS is measured without use of the convex hull or surface smoothing (**Figure 3.1**). Specifically, the R^2 between fractional area change (FAC) and LS is between 0.38-0.42 depending on the long-axis view. When the convex hull is used to fill in the voids created by papillary muscles, R^2 increases (0.83 - 0.89, **Figure 3.1**). Curve fitting of the endocardial surface leads to a further increase in R^2 (0.91 - 0.92, **Figure 3.1**). The increase in R^2 was statistically significant ($p < 0.05$) for all views.

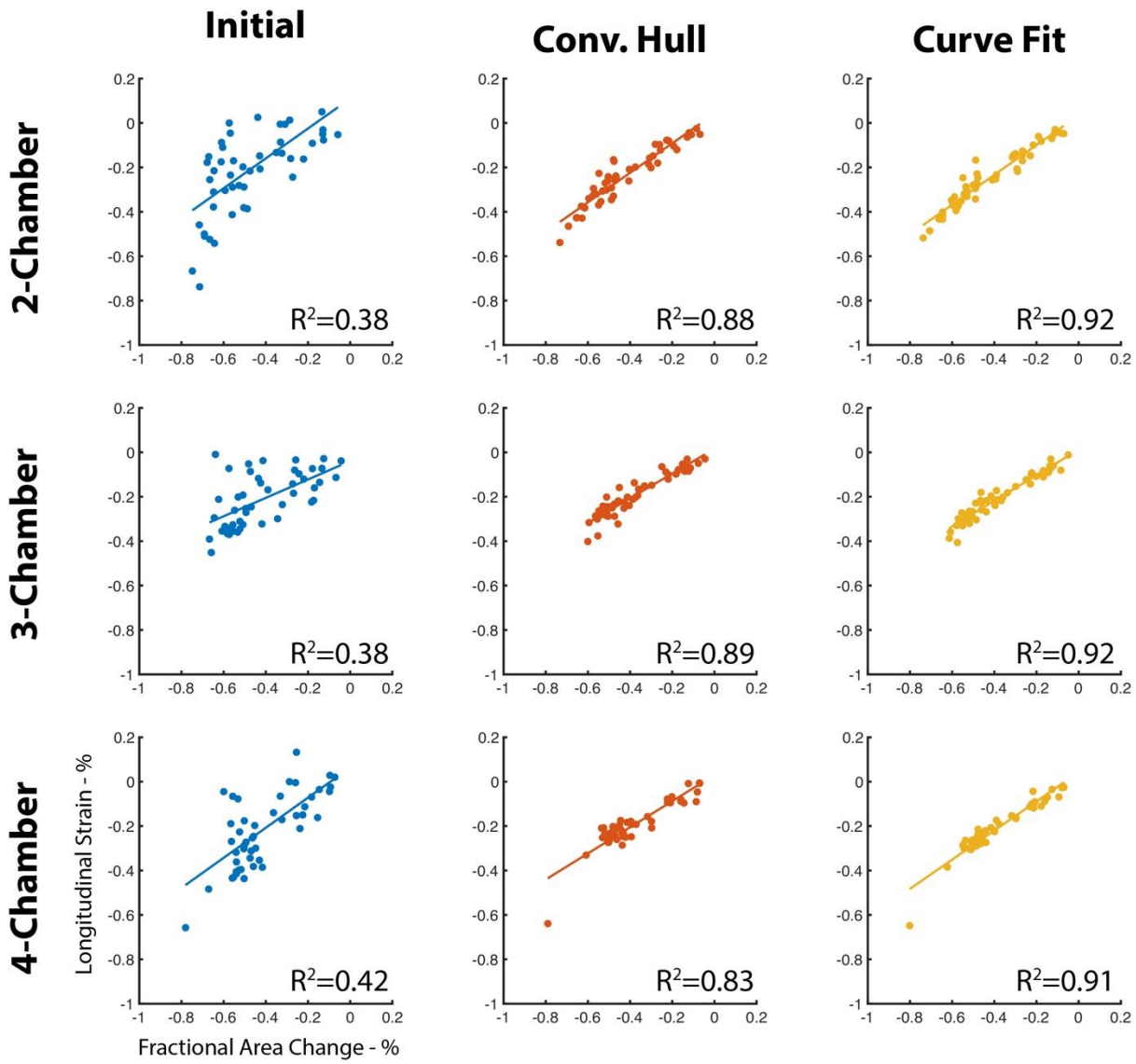

Figure 3.1: Agreement between LS and FAC increases with use of the convex hull and perimeter curve fitting.

3.3 Determination of LS Cutoffs and Classification Performance in Training Cohort

For all long-axis views, the area under the ROC curve using the convex hull and curve fitting was high (0.957 - 0.984. **Figure 3.2**) and the optimal threshold corresponded to a 100%

specificity performance, accuracy >91.7% and sensitivity between 84.2 and 90.0 percent. There was a small range of LS thresholds amongst LAX views with a higher cutoff identified for the 2CH view (-0.218) relative to the 3CH and 4CH views (-0.154 and -0.166, respectively). Per-patient performance (95.8% accuracy, 90.0% sensitivity, 100% specificity) was comparable to the values obtained for each long-axis view.

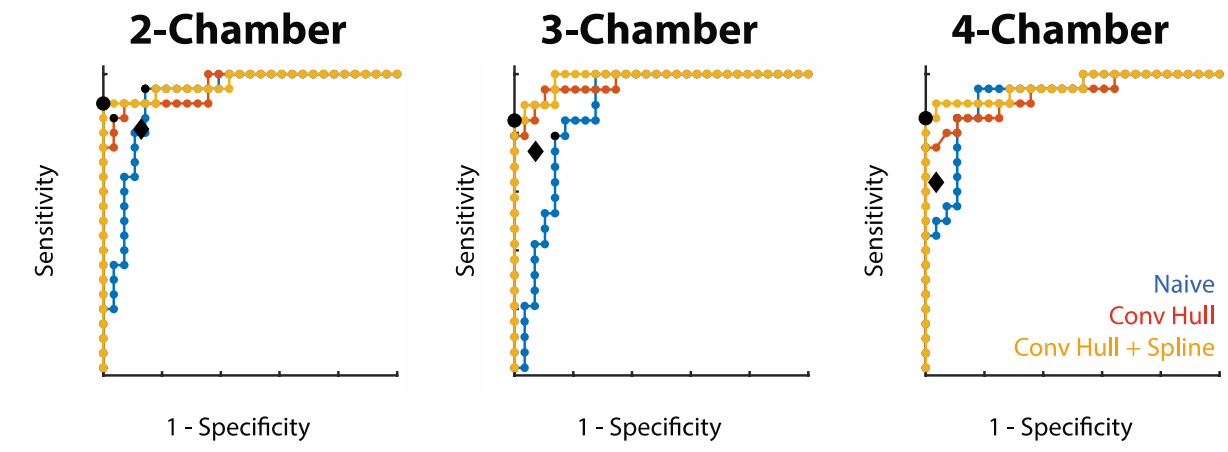

Figure 3.2: ROC curves for WMA classification using LS in the training cohort. Black dot shows optimal point in training cohort; black diamond shows performance of optimal cutoff in testing cohort.

We also evaluated the ability of a single threshold to classify WMA across all long-axis views. When pooled, LS thresholding had an area under the ROC of 0.965 and the use of -0.170 as the cutoff led to 92.4% accuracy, 83.0% sensitivity, and 100% specificity. This led to 95.8% accuracy, 90.0% sensitivity, and 100% specificity when classifying patients. Complete values are shown in **Table 3.2**.

Table 3.2: Use of training cohort for identification of LS cutoffs for WMA detection using the curve fitting approach. Thresh: optimal threshold identified for classification, AUC: area under the receiver operating characteristic curve, Sens: sensitivity, Spec: specificity, PPV: positive predictive value. 2CH: two-chamber view, 3CH: three-chamber view, 4CH: four-chamber view, LAX: long-axis view.

		Thresh	AUC	Acc	Sens	Spec	PPV
Individual Threshold	**2CH**	-0.218	0.970	93.8	90.0	100	100
	3CH	-0.154	0.984	91.7	84.2	100	100
	4CH	-0.166	0.957	91.7	85.0	100	100
	Per-LAX View	N/A	N/A	92.4	81.4	100	100
	Per-Patient			95.8	90.0	100	100
Single Threshold	**Per-LAX View**	-0.170	0.965	92.4	83.1	100	100
	Per-Patient		N/A	95.8	90.0	100	100

3.4 Per-study and Per-video Classification Performance in Testing Cohort

Using the convex hull and curve fitting approach, we then applied the thresholds identified in the training cohort to the testing population. The accuracy and specificity remained high (>83.0% and >87.1%, respectively) when each view was evaluated independently. Sensitivity ranged between 63.2% (4CH view) and 81.3% (2CH view). This led to an overall accuracy in classifying LAX views of 84.4% with a specificity of 92.0%. The use of a single threshold had similar performance (85.1% accuracy, 94.3% specificity). In both the individual and single threshold case, the per-patient accuracy was 83.0% in the testing cohort. Complete values are shown in **Table 3.3**.

Table 3.3: Performance of LS in the testing cohort using the curve-fitting approach. Thresh: optimal threshold identified for classification, AUC: area under the receiver operating characteristic curve, Sens: sensitivity, Spec: specificity, PPV: positive predictive value. 2CH: two-chamber view, 2CH: three-chamber view, 4CH: four-chamber view, LAX: long-axis view.

		Thresh	Acc	Sens	Spec	PPV
Individual Threshold	**2CH**	-0.218	85.1	81.3	87.1	76.5
	3CH	-0.154	85.1	73.7	92.9	87.5
	4CH	-0.166	83.0	63.2	96.4	92.3
	Per-LAX View	N/A	84.4	72.2	92.0	84.8
	Per-Patient		83.0	84.2	82.1	76.2
Single Threshold	**Per-LAX View**	-0.170	85.1	70.4	94.3	88.4
	Per-Patient		83.0	79.0	85.7	79.0

Fleiss's Kappa for 3 experts in testing cohort is 0.788, 0.855, 0.821 for 2-CH, 3-CH, 4-CH views respectively, 0.822 for all views, and 0.827 per patient. **Table 3.4** and **Table 3.5** show confusion matrix of LS classification of WMA, using individual and single threshold. When using individual threshold, Cohen's Kappa between LS and experts is 0.673, 0.683, 0.628 for 2-CH, 3-CH, 4-CH views respectively, 0.672 for all views, and 0.697 per patient. When using a single threshold, Cohen's Kappa between LS and experts is 0.744, 0.688, 0.585 for 2-CH, 3-CH, 4-CH views respectively, 0.672 for all views, and 0.693 per patient. This indicates substantial agreement between LS and expert classifications.

Table 3.4: Confusion matrix for 2-Chamber, 3-Chamber, 4-Chamber views, all views and per-study identification of WMA, using individual threshold. WMA+/-: presence/absence of WMA as determined by experts; LS+/-: presence/absence of WMA as classified by LS.

	2-Chamber		3-Chamber		4-Chamber		All views		Per patient	
	LS-	**LS+**	**LS-**	**LS+**	**LS-**	**LS+**	**LS-**	**LS+**	**LS-**	**LS+**
WMA-	27	4	26	2	27	1	82	5	23	4
WMA+	3	13	5	14	7	12	16	38	3	17

Table 3.5: Confusion matrix for 2-Chamber, 3-Chamber, 4-Chamber views, all views and per-study identification of WMA, using single threshold. WMA+/-: presence/absence of WMA as determined by experts; LS+/-: presence/absence of WMA as classified by LS.

	2-Chamber		3-Chamber		4-Chamber		All views		Per patient	
	LS-	**LS+**	**LS-**	**LS+**	**LS-**	**LS+**	**LS-**	**LS+**	**LS-**	**LS+**
WMA-	31	0	25	3	26	2	82	5	24	3
WMA+	5	11	4	15	7	12	16	38	4	16

3.5 MAPSE

Correlation between MAPSE from three different approaches and LV ejection fraction is shown in **Figure 3.3**. All three approaches showed moderate correlation with R^2 between 0.56 to 0.60. There is no significant difference between three approaches ($p>0.05$).

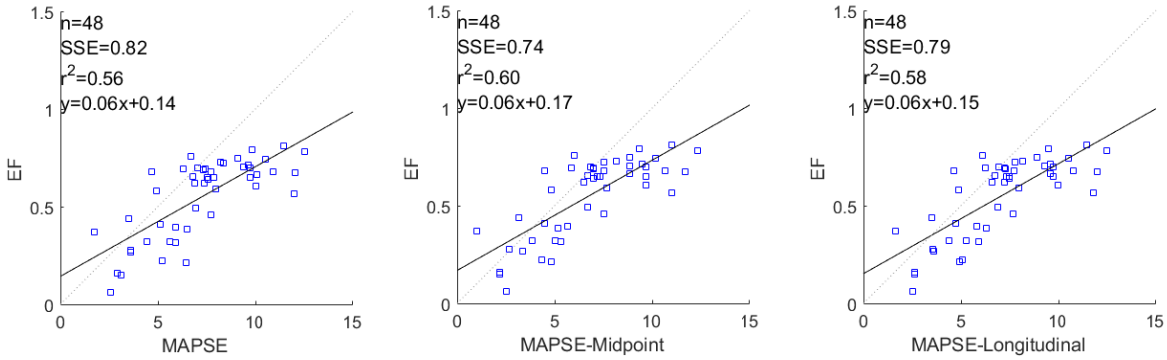

Figure 3.3: MAPSE correlation plot with EF

Since there is no significant difference between performance of the three approaches, we proceed to evaluate the utility of MAPSE in WMA classification using the conventional approach of MAPSE measurement. As shown in **Figure 3.4**, ROC for MAPSE has AUC of 0.852. The top left point of the ROC curve is selected as the optimal MAPSE threshold for classifying WMA. This threshold has 83.3% accuracy in the training cohort (75.0% sensitivity and 89.3% specificity). In the testing cohort, this threshold classifies WMA with 78.7% accuracy (70.0% sensitivity and 85.2% specificity).

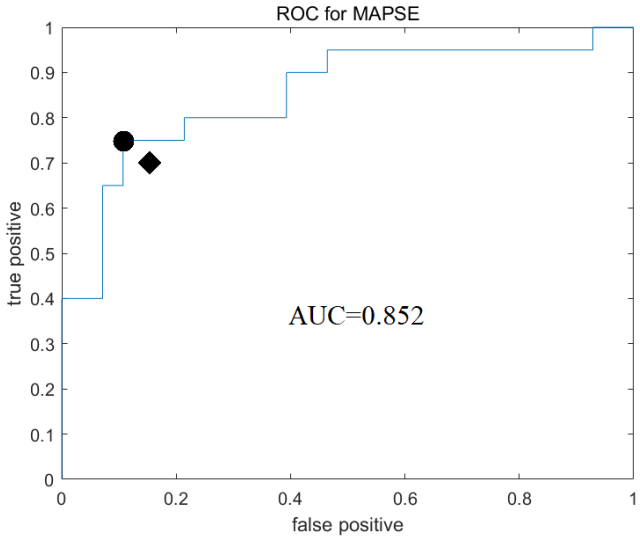

Figure 3.4: ROC plot for MAPSE in the training cohort. Optimal MAPSE cutoff for classifying WMA was determined by the top left point, marked by the black dot. Performance of this threshold in the testing cohort is marked with the black diamond.

Table 3.6: Use of training cohort for identification of MAPSE cutoffs for WMA detection and performance of MAPSE in the testing cohort using the conventional approach.

	Thresh	AUC	Accu	Sens	Spec
Training		0.852	83.3	75.0	89.3
	6.48				
Testing		-	78.7	70.0	85.2

Acknowledgements

Chapter 3, in part, has been submitted for publication of the material as it may appear in Frontiers, 2022, Hui Li; Zhennong Chen; Andrew M Kahn; Seth Kligerman; Hari K Narayan; Francisco J Contijoch. The thesis author was the primary researcher and author of this paper. Content of this chapter has, in part, been presented at SCCT.

CHAPTER 4 DISCUSSION

4.1 Conclusions

We demonstrate how deep learning (DL) segmentation of the left atrial and left ventricular bloodpools can be combined with automated prediction of the long-axis imaging planes to automatically calculate longitudinal shortening along each long-axis view and detect wall motion abnormalities. In this study, we applied the previously trained DL tool to our CT studies without retraining or refinement and developed steps to extract LS and MAPSE from the resulting data. To the best of our knowledge, this is the first study to automatically quantify LS and MAPSE along long-axis views from ECG-gated cardiac CT angiograms. To demonstrate the clinical utility, we evaluated the ability of automated LS and MAPSE to detect WMA. When applied to the testing cohort, the LS identified WMA with accuracy > 83.0% and specificity >92.9%.

A single LS threshold value of -17.0% had similar performance during the training phase as unique thresholds for each long-axis view and higher performance in the testing cohort. This LS cutoff is similar to those previously reported in other populations and with other imaging methods. In a meta-analysis of chemotherapy-induced cardiotoxicity, Oikonomou et al reviewed studies which had high-risk cutoff values of -21.0% to -13.8% [13]. Similarly, Kearney et al found LS in controls to be -21 ± 2% while patients with AS had LS between -18% and -15% depending on the AS severity [14] and Zhu et al found mortality in AS patients was higher in those with LS > -15.2% [15].

This method could add the clinical interpretation of cardiac CT angiograms by serving as an aid for expert readers. It is also likely that providing the LS score for each view is of value. For example, reporting the LS score along with the relevant cutoff would enable the expert to

gain a sense of both the prediction of the algorithm as well as the confidence of the prediction. Also, it is possible that a high sensitivity threshold provides more clinically useful predictions, especially if applied to patients in a screening type of setting. However, this utility is left for future studies.

While the development of the deep learning segmentation required specialized graphics hardware, the use of the DL and the subsequent LS processing can be easily incorporated into a clinical pipeline and can be readily performed on conventional computers.

4.2 MAPSE

When applied to the testing cohort, MAPSE identified WMA with 78.7% accuracy, 70.0% sensitivity and 85.2% specificity. This is a lower performance than identification with LS in the same patient cohort. From our current results, the use of MAPSE did not bring additional clinical utility compared to LS. However, having MAPSE measured in an automated pipeline enables comparison with patient's history if previous measurements were done in MAPSE. Since MAPSE is less dependent on imaging quality, it can be tested in studies with suboptimal image quality to evaluate the utility of automated MAPSE measurement in this kind of studies. However, this utility is left for future studies.

4.3 Limitations

Our study had several limitations. First, the DL segmentation failed to produce accurate segmentations and/or long-axis imaging planes in 5/100 patients (n=2 in the training cohort and n=3 in the testing cohort). The 95% success rate is likely sufficient for clinical use, especially given that the result of the DL blood pool segmentation and long-axis planes can be displayed to the reader for review. Further, it is likely that the failure rate would decrease if a larger, more diverse, training dataset was used for the development of the DL method. In the work by Chen et

al, only 100 patients were used for training (with 2 CT frames per patient) [10]. Further, our approach identifies WMA using LS since the DL segmentation only provides endocardial boundary information. If epicardial segmentations were available, then other metrics such as regional wall thickening could be measured. Lastly, LS is correlated with other metrics of function such as FAC and EF. Our study was not designed nor powered to identify whether LS is a better independent predictor of WMA than these other metrics but others have documented the utility of LS [17, 19].

4.4 Performance of LS Classification with Expert Concordance/Discordance

During the expert identification of WMA, we noticed concordance and discordance between three experts' WMA labels. Our study is based on agreement of 2 or more experts, and did not differentiate between cases of concordance (where all three experts agreed on a WMA label) and discordance (where disagreement existed among the experts). LS classification may have different performance in these two groups, and in cases of discordance, automated LS classification may be helpful in complementation to manual classification. Due to the small sample size of discordance in our study (18 views and 6 patients in the testing cohort), we are unable to determine if there is difference in performance between the concordant and discordant cases. Further studies with larger sample may provide more evidence.

4.5 LS Estimation may be Limited due to Foreshortening

Foreshortening happens when the LAX imaging plane fails to cross the apex. This distorts the image and has been shown in speckle tracking echocardiography to induce significant difference in strain measurement [36]. Our algorism currently relies on the DL framework to generate accurate LAX imaging planes, and does not perform detection of foreshortening. This could explain why some WMA were not detected by our approach.

In conclusion, longitudinal shortening, typically measured with MRI or echocardiography, has been previously shown to be diagnostic and prognostic of several patient populations. We leverage a recently developed deep learning approach to automate LS estimation in ECG-gated CT angiograms and demonstrate that LS can be used to detect wall motion abnormalities. Our algorism produces LS and MAPSE estimations in an average of 14 seconds for each patient on a laptop computer, and we are confident that on a computer dedicated for image processing, it will achieve the results in less than a few seconds. Since the process is completely automated, it can be incorporated into a cardiac CT pipeline in clinical setting to provide these additional parameters.

Acknowledgements

Chapter 4, in part, has been submitted for publication of the material as it may appear in Frontiers, 2022, Hui Li; Zhennong Chen; Andrew M Kahn; Seth Kligerman; Hari K Narayan; Francisco J Contijoch. The thesis author was the primary researcher and author of this paper.

REFERENCES

[1] Douglas PS, Hoffmann U, Patel MR, Mark DB, Al-Khalidi HR, Cavanaugh B, Cole J, Dolor RJ, Fordyce CB, Huang M, Khan MA, Kosinski AS, Krucoff MW, Malhotra V, Picard MH, Udelson JE, Velazquez EJ, Yow E, Cooper LS, Lee KL; PROMISE Investigators. Outcomes of anatomical versus functional testing for coronary artery disease. N Engl J Med. 2015 Apr 2;372(14):1291-300.

[2] The SCOT-HEART Investigators. Coronary CT Angiography and 5-Year Risk of Myocardial Infarction. N Engl J Med. 2018 Sep 6;379(10):924–33.

[3] Cardiac Computed Tomography Writing Group, Taylor AJ, Cerqueira M, Hodgson JMcB, Mark D, Min J, O'Gara P and Rubin GD.
ACCF/SCCT/ACR/AHA/ASE/ASNC/NASCI/SCAI/SCMR 2010 Appropriate Use Criteria for Cardiac Computed Tomography: A Report of the American College of Cardiology Foundation Appropriate Use Criteria Task Force, the Society of Cardiovascular Computed Tomography, the American College of Radiology, the American Heart Association, the American Society of Echocardiography, the American Society of Nuclear Cardiology, the North American Society for Cardiovascular Imaging, the Society for Cardiovascular Angiography and Interventions, and the Society for Cardiovascular Magnetic Resonance. Circulation [Internet]. 2010 Nov 23 [cited 2022 Jul 11];122(21). Available from:
https://www.ahajournals.org/doi/10.1161/CIR.0b013e3181fcae66

[4] Rossi A, Dharampal A, de Feyter PJ. Coronary CT angiography for patients with suspected coronary artery disease. Heart. 2014 Jun;100(12):976-84.

[5] Tavakoli V, Sahba N. Cardiac motion and strain detection using 4D CT images: comparison with tagged MRI, and echocardiography. Int J Cardiovasc Imaging. 2014 Jan;30(1):175–84.

[6] Buss SJ, Schulz F, Mereles D, Hosch W, Galuschky C, Schummers G, Stapf D, Hofmann N, Giannitsis E, Hardt SE, Kauczor HU, Katus HA, Korosoglou G. Quantitative analysis of left ventricular strain using cardiac computed tomography. Eur J Radiol. 2014 Mar;83(3):e123-30.

[7] Kaniewska M, Schuetz GM, Willun S, Schlattmann P, Dewey M. Noninvasive evaluation of global and regional left ventricular function using computed tomography and magnetic resonance imaging: a meta-analysis. Eur Radiol. 2017 Apr;27(4):1640–59.

[8] Pourmorteza A, Chen MY, van der Pals J, Arai AE, McVeigh ER. Correlation of CT-based regional cardiac function (SQUEEZ) with myocardial strain calculated from tagged MRI: an experimental study. Int J Cardiovasc Imaging. 2016 May;32(5):817–23.

[9] Contijoch FJ, Groves DW, Chen Z, Chen MY, McVeigh ER. A novel method for evaluating regional RV function in the adult congenital heart with low-dose CT and SQUEEZ processing. Int J Cardiol. 2017 Dec 15;249:461-466.

[10] Chen Z, Rigolli M, Vigneault DM, Kligerman S, Hahn L, Narezkina A, Craine A, Lowe K, Contijoch F. Automated cardiac volume assessment and cardiac long- and short-axis imaging plane prediction from electrocardiogram-gated computed tomography volumes enabled by deep learning. Eur Heart J Digit Health. 2021 Mar 22;2(2):311-322.

[11] Cheitlin MD, Armstrong WF, Aurigemma GP, Beller GA, Bierman FZ, Davis JL, Douglas PS, Faxon DP, Gillam LD, Kimball TR, Kussmaul WG, Pearlman AS, Philbrick JT, Rakowski H, Thys DM, Antman EM, Smith SC Jr, Alpert JS, Gregoratos G, Anderson JL, Hiratzka LF, Hunt SA, Fuster V, Jacobs AK, Gibbons RJ, Russell RO; American College of Cardiology; American Heart Association; American Society of Echocardiography. ACC/AHA/ASE 2003 guideline update for the clinical application of echocardiography: summary article: a report of the American College of Cardiology/American Heart Association Task Force on Practice Guidelines (ACC/AHA/ASE Committee to Update the 1997 Guidelines for the Clinical Application of Echocardiography). Circulation. 2003 Sep 2;108(9):1146-62.

[12] American College of Cardiology Foundation Task Force on Expert Consensus Documents, Hundley WG, Bluemke DA, Finn JP, Flamm SD, Fogel MA, Friedrich MG, Ho VB, Jerosch-Herold M, Kramer CM, Manning WJ, Patel M, Pohost GM, Stillman AE, White RD, Woodard PK. ACCF/ACR/AHA/NASCI/SCMR 2010 expert consensus document on cardiovascular magnetic resonance: a report of the American College of Cardiology Foundation Task Force on Expert Consensus Documents. J Am Coll Cardiol. 2010 Jun 8;55(23):2614-62.

[13] Oikonomou EK, Kokkinidis DG, Kampaktsis PN, Amir EA, Marwick TH, Gupta D, Thavendiranathan P. Assessment of Prognostic Value of Left Ventricular Global Longitudinal Strain for Early Prediction of Chemotherapy-Induced Cardiotoxicity: A Systematic Review and Meta-analysis. JAMA Cardiol. 2019 Oct 1;4(10):1007-1018.

[14] Kearney LG, Lu K, Ord M, Patel SK, Profitis K, Matalanis G, Burrell LM, Srivastava PM. Global longitudinal strain is a strong independent predictor of all-cause mortality in patients with aortic stenosis. Eur Heart J Cardiovasc Imaging. 2012 Oct;13(10):827-33.

[15] Zhu D, Ito S, Miranda WR, Nkomo VT, Pislaru SV, Villarraga HR, Pellikka PA, Crusan DJ, Oh JK. Left Ventricular Global Longitudinal Strain Is Associated With Long-Term Outcomes in Moderate Aortic Stenosis. Circ Cardiovasc Imaging. 2020 Apr;13(4):e009958.

[16] Phelan D, Collier P, Thavendiranathan P, Popović ZB, Hanna M, Plana JC, Marwick TH, Thomas JD. Relative apical sparing of longitudinal strain using two-dimensional speckle-tracking echocardiography is both sensitive and specific for the diagnosis of cardiac amyloidosis. Heart. 2012 Oct;98(19):1442-8.

[17] Russo C, Jin Z, Sera F, Lee ES, Homma S, Rundek T, Elkind MS, Sacco RL, Di Tullio MR. Left Ventricular Systolic Dysfunction by Longitudinal Strain Is an Independent Predictor of Incident Atrial Fibrillation: A Community-Based Cohort Study. Circ Cardiovasc Imaging. 2015 Aug;8(8):e003520.

[18] Sengeløv M, Jørgensen PG, Jensen JS, Bruun NE, Olsen FJ, Fritz-Hansen T, Nochioka K, Biering-Sørensen T. Global Longitudinal Strain Is a Superior Predictor of All-Cause Mortality in Heart Failure With Reduced Ejection Fraction. JACC Cardiovasc Imaging. 2015 Dec;8(12):1351-1359.

[19] Reindl M, Tiller C, Holzknecht M, Lechner I, Beck A, Plappert D, Gorzala M, Pamminger M, Mayr A, Klug G, Bauer A, Metzler B, Reinstadler SJ. Prognostic Implications of Global Longitudinal Strain by Feature-Tracking Cardiac Magnetic Resonance in ST-Elevation Myocardial Infarction. Circ Cardiovasc Imaging. 2019 Nov;12(11):e009404.

[20] Mele D, Pasanisi G, Heimdal A, Cittanti C, Guardigli G, Levine RA, Sutherland G, Ferrari R. Improved recognition of dysfunctioning myocardial segments by longitudinal strain rate versus velocity in patients with myocardial infarction. J Am Soc Echocardiogr. 2004 Apr;17(4):313-21.

[21] Cimino S, Canali E, Petronilli V, Cicogna F, De Luca L, Francone M, Sardella G, Iacoboni C, Agati L. Global and regional longitudinal strain assessed by two-dimensional speckle tracking echocardiography identifies early myocardial dysfunction and transmural extent of myocardial scar in patients with acute ST elevation myocardial infarction and relatively preserved LV function. Eur Heart J Cardiovasc Imaging. 2013 Aug;14(8):805-11.

[22] Carluccio E, Tommasi S, Bentivoglio M, Buccolieri M, Prosciutti L, Corea L. Usefulness of the severity and extent of wall motion abnormalities as prognostic markers of an adverse outcome after a first myocardial infarction treated with thrombolytic therapy. Am J Cardiol. 2000 Feb 15;85(4):411-5.

[23] Møller JE, Hillis GS, Oh JK, Reeder GS, Gersh BJ, Pellikka PA. Wall motion score index and ejection fraction for risk stratification after acute myocardial infarction. Am Heart J. 2006 Feb;151(2):419-25.

[24] Cicala S, de Simone G, Roman MJ, Best LG, Lee ET, Wang W, Welty TK, Galloway JM, Howard BV, Devereux RB. Prevalence and prognostic significance of wall-motion abnormalities in adults without clinically recognized cardiovascular disease: the Strong Heart Study. Circulation. 2007 Jul 10;116(2):143-50.

[25] Chen C, Qin C, Qiu H, Tarroni G, Duan J, Bai W, Rueckert D. Deep Learning for Cardiac Image Segmentation: A Review. Front Cardiovasc Med. 2020 Mar 5;7:25.

[26] Litjens G, Ciompi F, Wolterink JM, de Vos BD, Leiner T, Teuwen J, Išgum I. State-of-the-Art Deep Learning in Cardiovascular Image Analysis. JACC Cardiovasc Imaging. 2019 Aug;12(8 Pt 1):1549-1565.

[27] Bernard O, Lalande A, Zotti C, Cervenansky F, Yang X, Heng PA, Cetin I, Lekadir K, Camara O, Gonzalez Ballester MA, Sanroma G, Napel S, Petersen S, Tziritas G, Grinias E, Khened M, Kollerathu VA, Krishnamurthi G, Rohe MM, Pennec X, Sermesant M, Isensee F, Jager P, Maier-Hein KH, Full PM, Wolf I, Engelhardt S, Baumgartner CF, Koch LM, Wolterink

JM, Isgum I, Jang Y, Hong Y, Patravali J, Jain S, Humbert O, Jodoin PM. Deep Learning Techniques for Automatic MRI Cardiac Multi-Structures Segmentation and Diagnosis: Is the Problem Solved? IEEE Trans Med Imaging. 2018 Nov;37(11):2514-2525.

[28] Vigneault DM, Xie W, Ho CY, Bluemke DA, Noble JA. Ω-Net (Omega-Net): Fully automatic, multi-view cardiac MR detection, orientation, and segmentation with deep neural networks. Medical Image Analysis. 2018 Aug;48:95–106.

[29] Cerqueira MD, Weissman NJ, Dilsizian V, Jacobs AK, Kaul S, Laskey WK, Pennell DJ, Rumberger JA, Ryan T, Verani MS; American Heart Association Writing Group on Myocardial Segmentation and Registration for Cardiac Imaging. Standardized myocardial segmentation and nomenclature for tomographic imaging of the heart. A statement for healthcare professionals from the Cardiac Imaging Committee of the Council on Clinical Cardiology of the American Heart Association. Circulation. 2002 Jan 29;105(4):539-42.

[30] Bergenzaun L, Ohlin H, Gudmundsson P, Willenheimer R, Chew MS. Mitral annular plane systolic excursion (MAPSE) in shock: a valuable echocardiographic parameter in intensive care patients. Cardiovasc Ultrasound. 2013 May 30;11:16.

[31] Magdy G, Hamdy E, Elzawawy T, Ragab M. Value of mitral annular plane systolic excursion in the assessment of contractile reserve in patients with ischemic cardiomyopathy before cardiac revascularization. Indian Heart J. 2018 May-Jun;70(3):373-378.

[32] Mansell DS, Frank EG, Kelly NS, Agostinho-Hernandez B, Fletcher J, Bruno VD, Sammut E, Chiribiri A, Johnson T, Ascione R, Bartlett JW, Gill HS, Fraser KH, Cookson AN. Comparison of the within-reader and inter-vendor agreement of left ventricular circumferential strains and volume indices derived from cardiovascular magnetic resonance imaging. PLoS One. 2020 Dec 15;15(12):e0242908.

[33] Lee ETY. Choosing nodes in parametric curve interpolation. Computer-Aided Design. 1989 Jul;21(6):363–70.

[34] Xue H, Artico J, Davies RH, Adam R, Shetye A, Augusto JB, Bhuva A, Fröjdh F, Wong TC, Fukui M, Cavalcante JL, Treibel TA, Manisty C, Fontana M, Ugander M, Moon JC, Schelbert EB, Kellman P. Automated In-Line Artificial Intelligence Measured Global Longitudinal Shortening and Mitral Annular Plane Systolic Excursion: Reproducibility and Prognostic Significance. J Am Heart Assoc. 2022 Feb 15;11(4):e023849.

[35] Fleiss JL. Measuring nominal scale agreement among many raters. Psychological Bulletin. 1971;76(5):378–82.

[36] Tarr A, Stöbe S, Trache T, Kluge JG, Varga A, Pfeiffer D, Hagendorff A. The impact of foreshortening on regional strain--a comparison of regional strain evaluation between speckle tracking and tissue velocity imaging. Ultraschall Med. 2013 Oct;34(5):446-53.